

Tailoring sub-Doppler spectra of thermal atoms with a dielectric optical metasurface chip

Dengke Zhang* and Chen Qing

School of Instrumentation and Optoelectronic Engineering, Beihang University, Beijing 100191, China

Compact and robust structures to precisely control and acquire atomic spectra are increasingly important for the pursuit of widespread applications. Sub-Doppler responses of thermal atoms are critical in constructing high-precision devices and systems. In this study, we designed a nanograting metasurface specifically for atomic rubidium vapor and integrated it into a miniature vapor cell. Using the metasurface with built-in multifunctional controls for light, we established pump-probe atomic spectroscopy and experimentally observed sub-Doppler responses at low incident power. Moreover, the sub-Doppler lineshape can be tailored by varying the incident polarization state. The spectrum transformation from absorption to transparency was observed. Using one of the sharp responses, laser stabilization with a stability of 3×10^{-10} at 2 s can be achieved. Our work reveals the effective control of atomic spectra with optical metasurface chips, which may have great potential for future developments in fundamental optics and novel optical applications.

I. INTRODUCTION

Atomic-spectrum-based devices or systems such as atomic frequency standards and clocks,[1–3] atomic gyroscopes,[4, 5] and atomic magnetometers,[6, 7] have been widely used in various fields, including navigation and communications,[5, 8] precision measurements,[9, 10] and biological imaging.[11] In general, according to the developed technology, two types of atoms are applied: the cold atom and the thermal atomic vapor. The atomic spectra undoubtedly play a critical role in both application technologies. To achieve a high-performance device, precise control and acquisition of atomic spectra are indispensable, particularly when capturing atomic responses of hyperfine structures. Although this may not pose major challenges for the cold atoms, intricate control and implementation processes hinder their widespread utilization. Atom vapor is easy to obtain, but the atomic responses are significantly broadened due to the Doppler effect experienced by thermal atoms, which complicates the process of capturing accurate atomic spectra and makes it difficult to achieve the desired precision. To obtain sub-Doppler spectra, the pump-probe configuration is typically employed using saturation absorption or velocity selective optical pumping (VSOP).[12–14] In addition, sub-natural responses such as electromagnetically induced absorption (EIA) and transparency (EIT) can be observed by controlling the state of polarization (SOP) of the pump and probe beams.[15–21] The SOP of light is typically adjusted using bulky optical components of cascaded polarizers and waveplates. Thus, the optical setups for SOP manipulation tend to be large and unstable.

In recent years, optical metasurfaces with nanostructures at subwavelength scales have been rapidly developed and enabled control over the amplitude,[22] phase,[23]

propagation direction,[24] and polarization of transmitted and reflected light.[25] This development has brought a range of applications such as superlenses, holograms, sensing, and communications.[26, 27] Furthermore, optical metasurfaces have distinctive characteristics, such as the capability to simultaneously manipulate the amplitude, phase, and polarization, which are not attainable through conventional optical elements.[28–31] The emergence of nanostructured optical metasurfaces marked a significant development in modern photonics, since these elements can supplant or surpass the capabilities of conventional optics. Incorporating carefully engineered nanophotonic structures can help integrate diverse light beam manipulations into a compact chip. Consequently, a metasurface chip can be developed to permit accurate manipulation of the intensities and SOPs of light for the pump-probe configurations in atomic spectroscopy. Recently, there have been several reports on the combination of metasurfaces with thermal atoms for applications such as optical imaging,[32] measurement,[33–36] and laser cooling,[37, 38] or theoretical investigation of atom–surface interaction.[39, 40] However, the regulation of atomic spectra using metasurfaces has not been extensively explored.

In this work, we designed a nanograting metasurface with an operating wavelength of 780 nm, which corresponds to the D2 line of rubidium (Rb) atoms. The optical metasurface chip was engineered to achieve polarization-dependent reflection coefficients and phase shifts in reflected light. In particular, the transverse magnetic (TM) polarized light exhibits high reflectivity, whereas the transverse electric (TE) polarized light maintains a low reflectivity. The pump-probe configuration can be created by packaging the metasurface chip at the rear of the vapor cell, where the incoming light serves as the probe beam, and the reflected light functions as the pump beam. The intensity and SOP of the pump beam can be adjusted by altering the intensity or SOP of the incident beam. Experimentally, the sub-Doppler spectra were observed,

* dkzhang@buaa.edu.cn

and its lineshape could be modified by varying the SOP of the incident light at a low intensity. The laser stabilization was demonstrated, and stability of 3×10^{-10} at 2 s was achieved using one of the sub-Doppler transparent responses.

II. RESULTS

A. Hybrid metasurface-atomic-vapor device

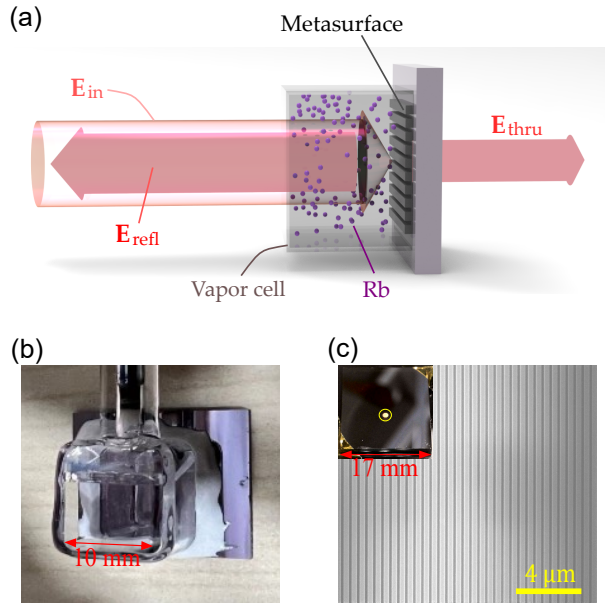


Figure 1. Diagram of the operation principle and photograph of the hybrid vapor cell. a) Schematic of the vapor cell constructed by a small cubic glass chamber, which was sealed by the designed metasurface chip. The incident light enters the vapor cell through the glass window, interacts with rubidium atoms, and shines on the metasurface. The reflected light induced by the metasurface returns to the vapor and interacts with the atoms again. A “pump-probe” configuration of the photon-atom interaction can be built using the metasurface. b) Photograph of a fabricated hybrid vapor cell assembled by a cubic glass chamber and a metasurface chip. c) Scanning electron microscope image of the grating structure of the metasurface. The inset shows a photograph of the metasurface chip.

Our hybrid metasurface-atomic-vapor device is schematically illustrated in Fig. 1a. The device consists of an all-dielectric optical metasurface chip, which is composed of silicon nanogratings on a borosilicate glass substrate. A cubic quartz chamber was bonded to this metasurface chip using a low-vapor-pressure resin sealant. Then, a rubidium (Rb) dispenser pill was inserted, and the chamber was successively evacuated and sealed. Finally, the Rb atoms were released by focusing a 5 W semiconductor laser at 915 nm onto the pill for a time duration of 15 s.

The inner length of the cubic vapor cell was 10 mm, and Fig. 1b shows a photograph of the hybrid cell.

As shown in Fig. 1a, the light beam was injected from the front transparent window into the vapor cell, interacted with the thermal atoms, and scattered by the nanogratings on the back chip. The reflected light returned to the vapor and interacted with the atoms again. Consequently, at the normal incidence, an atom can see both incident light and reflected light from opposite directions. Using the birefringence and dichroism of the metasurface, the intensity and SOP of the reflected light can be adjusted by changing the incident light’s SOP. Using this adjustable pump-probe configuration, the optical coherence of atoms can be altered by tuning the interaction between light and atoms, which changes their response. In principle, these modulations will be observed in both reflectance and transmittance spectra of the vapor cells.

B. Design and characterization of metasurface

In this hybrid vapor-cell-based pump-probe configuration, the incident light is called the “probe,” and the reflected light is called the “pump.” To maximize pumping, the metasurface must have high reflectivity. Generally, metal-structured metasurfaces can have very high reflectivity, but there is no transmitted light. The spectrum of the probe light will help extract information of the interaction between light and atoms. With these considerations, we adopted an all-dielectric metasurface structure with high-contrast gratings.[41–43] The high-contrast gratings can offer a high reflectivity while enabling some light to pass through the cells. In fact, by changing the SOP of the incident light, both reflectivity and transmissivity can be adjusted using these nanogratings. In our device, the high-contrast gratings were constructed from silicon wires on a glass substrate. The absorption of these thin silicon wires is weak for 780 nm incident light. We performed simulations to obtain a high reflectivity for TM polarized light using the rigorous coupled wave analysis (RCWA) method. The gratings were designed 441 nm in pitch with a duty ratio of 0.65, and the height of the silicon wires was 290 nm. Fig. 1c shows a scanning electron microscope (SEM) image of the gratings, and the inset displays the corresponding metasurface chip, where a 1-mm-diameter circular area with the fabricated gratings was located in the center of the chip.

The metasurface device was characterized by measuring the reflectivity at different incident angles. The incident light was linearly polarized by a polarizer; then, the direction of polarization was tuned using a half-wave plate as shown in Fig. 2a. The incident beam finally shone on the metasurface with a focusing lens, and the reflected beam was detected by a photodiode (PD). To vary the incident angle, we used two electronically controlled turnplates to simultaneously rotate the metasurface chip and PD. These

all-dielectric gratings exhibited two eigenpolarization responses, which corresponded to the TM and TE polarized incident lights (see the left inset of Fig. 2a). Figure 2b shows the zeroth-order reflection responses with respect to the incident angle. The right inset of Fig. 2a shows the definition of the incident angle θ . Figure 2b shows that the measured reflectivities for both TM and TE polarized incident lights are consistent with the simulated results. The results indicate that a high reflectivity of 0.93 for TM polarized light can be obtained at the normal incidence using the fabricated metasurface. Meanwhile, the measured reflectance is only 0.16 for TE polarized light. In addition, the phase difference of the reflected light between these two polarizations is assessed by SOP measurement as 65° . Therefore, it is possible to adjust the intensity and SOP of the reflected light in a wide range by changing the SOP of the incident light.

C. Theoretical analysis of the optical responses of the hybrid system

As described for the designed metasurface, the reflection and transmission responses for TM and TE polarized lights are different, i.e., there is an apparent birefringence. Specifically, the intensity and SOP of the reflected light could be dramatically adjusted by varying the polarization of incident light. Our designed metasurface has TM and TE polarizations as its eigenpolarizations, i.e., any polarized incident light can be separated into two such polarized components for independent treatment, as shown in Fig. 3a. In our assumptions, the linearly polarized incident light was denoted by $\mathbf{E}_{\text{in}} = E_0(\cos \phi \hat{\mathbf{e}}_x + \sin \phi \hat{\mathbf{e}}_y)$, where E_0 is the amplitude of light, ϕ is the polarization angle, and $\hat{\mathbf{e}}_x(\hat{\mathbf{e}}_y)$ are the normalized TM (TE) polarized states. Moreover, the reflected light of the metasurface can be expressed as $\mathbf{E}_{\text{rMS}} = r_x E_0 \cos \phi \hat{\mathbf{e}}_x + r_y E_0 \sin \phi \hat{\mathbf{e}}_y$, where $r_x(r_y)$ are the complex reflection coefficients of the TM (TE) polarized components. The reflected light can be transferred to an elliptically polarized light, which is induced by the phase difference between r_x and r_y . Considering the interactions of atoms with both incident and reflected lights, we selected the propagation direction (z -direction) of light as the quantization axis for atoms. For simplicity, the incident light \mathbf{E}_{in} and reflected light \mathbf{E}_{rMS} are rewritten with circular polarization states as

$$\mathbf{E}_{\text{in}} = \frac{E_0}{\sqrt{2}} [(\cos \phi + i \sin \phi) \hat{\mathbf{e}}_- + (i \cos \phi + \sin \phi) \hat{\mathbf{e}}_+], \quad (1)$$

$$\mathbf{E}_{\text{rMS}} = \frac{E_0}{\sqrt{2}} [(r_x \cos \phi + i r_y \sin \phi) \hat{\mathbf{e}}_- + (i r_x \cos \phi + r_y \sin \phi) \hat{\mathbf{e}}_+], \quad (2)$$

where $\hat{\mathbf{e}}_{-(+)} = [\hat{\mathbf{e}}_{x(y)} - i \hat{\mathbf{e}}_{y(x)}] / \sqrt{2}$ are the spherical bases. Furthermore, \mathbf{E}_{in} and \mathbf{E}_{rMS} can be redefined as $\mathbf{E}_{\text{in}} =$

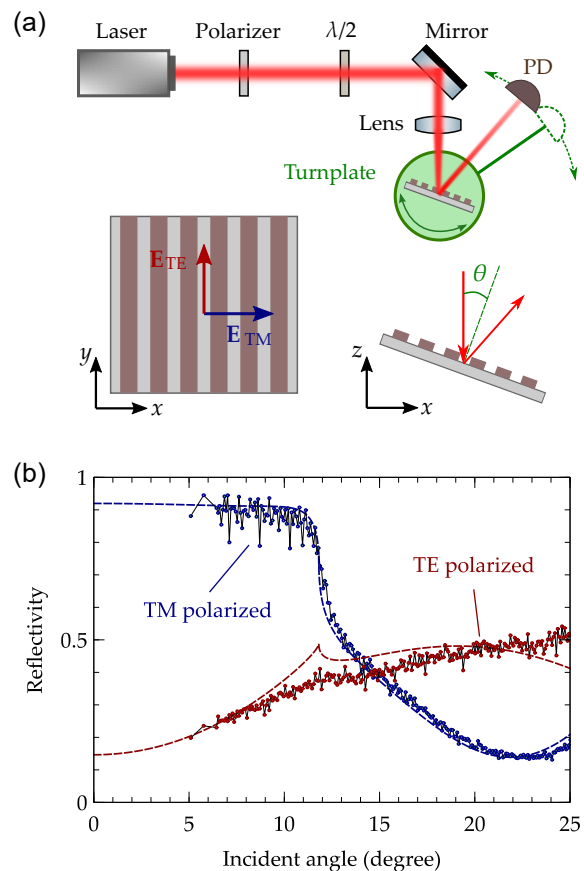


Figure 2. Schematic of the experimental setup and optical responses of the metasurface. a) Experimental setup to measure the reflectivity of the metasurface illuminated by TM and TE polarized lights at different incident angles. $\lambda/2$: half-wave plate; PD: photodiode. The left inset sketches the field directions of TM and TE polarized light. The right inset describes the defined incident angle. b) Measured and simulated zeroth-order reflectivities for both TM and TE polarized incident lights as a function of the incident angles. The measurement was performed at $\theta > 5^\circ$ due to the occlusion between incoming and reflected lights in the rotating setup. The dashed curves show the simulation results, and the dot-marker curves show the measured results.

$E_0(a_- \hat{\mathbf{e}}_- + a_+ \hat{\mathbf{e}}_+) / \sqrt{2}$ and $\mathbf{E}_{\text{rMS}} = E_0(b_- \hat{\mathbf{e}}_- + b_+ \hat{\mathbf{e}}_+) / \sqrt{2}$, respectively. The expressions of coefficients a_{\pm} and b_{\pm} can be obtained using equations (1) and (2). In this work, we study the atomic spectra for the D2 transitions of Rb atoms. For simplicity, we used $F_g = 1 \rightarrow F_e = 0, 1, 2$ transitions of ^{87}Rb atoms to explain the modeling and computation process. Figure 3b shows the energy level diagram of the D2 line of the ^{87}Rb atoms. The purple solid and green dashed arrows represent the transitions caused by the pump and probe beams, respectively. As displayed in Fig. 3b, both σ^{\pm} transitions can be excited by the two light beams, since their fields are not purely circularly polarized.

In the atomic vapor, Rb atoms moving with velocity v along the light propagation direction experience the

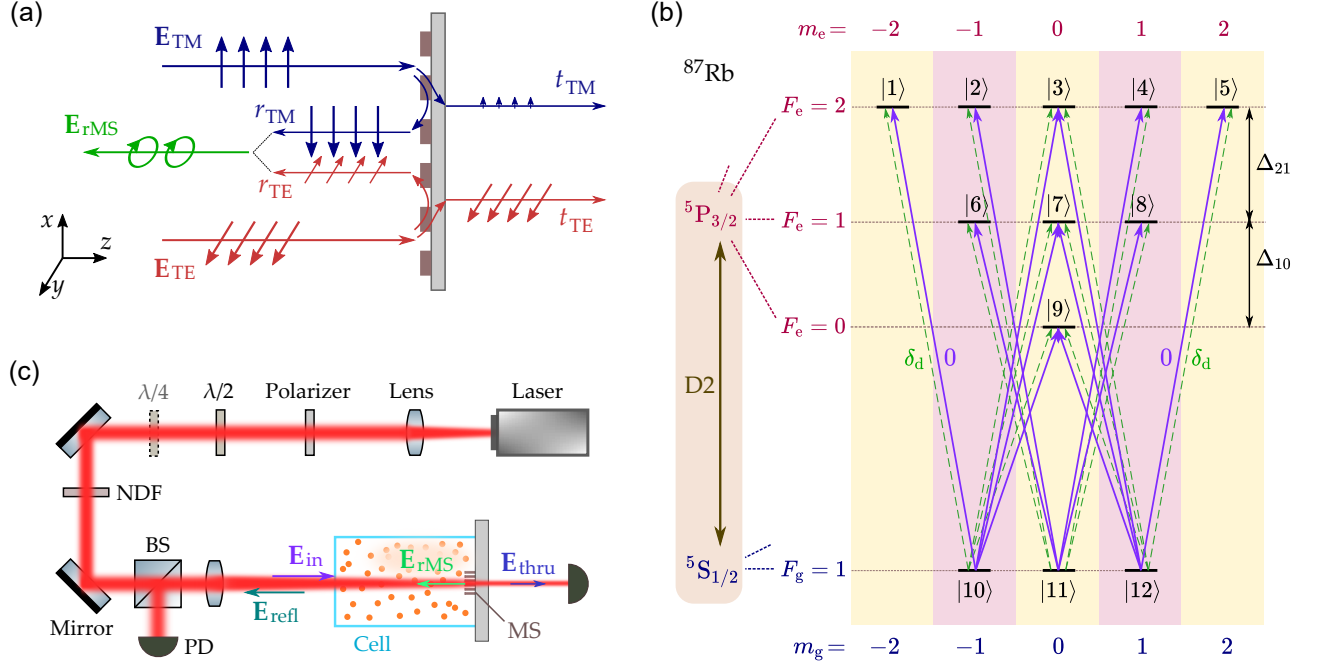


Figure 3. Modeling for the hybrid metasurface-atomic-vapor device and experimental setup. a) Sketch of TM and TE polarized incident light scattered by the metasurface. b) Energy level diagram of the D2 line of ⁸⁷Rb atoms with degenerate Zeeman sublevels. The levels of $F_g = 2$ and $F_e = 3$ are not shown in this diagram. c) Schematic description of the experimental setup. $\lambda/4$: quarter-wave plate; NDF: neutral density filter; BS: beam splitter; MS: metasurface.

optical frequencies of the probe and pump beams as $\omega_{\text{pr}} = \omega + kv$ and $\omega_{\text{pu}} = \omega - kv$, respectively, where ω is the optical angular frequency, and k is the wave number of the laser beam. We solve the following density matrix equation in a rotating frame with frequency ω_{pu} :

$$\dot{\rho} = -\frac{i}{\hbar}[H_0 + V, \rho] + (\dot{\rho})_{\text{sp}}, \quad (3)$$

where ρ is the density operator, \hbar is the reduced Planck constant, H_0 (V) is the bare atomic (interaction) Hamiltonian, and $(\dot{\rho})_{\text{sp}}$ denotes the dissipation process. The bare atomic Hamiltonian H_0 contains all transition-related degenerate Zeeman sublevels, which are marked by |1> to |12> in Fig. 3b. The interaction Hamiltonian V contains the couplings of atoms with both pump and probe beams. We can derive an effective electric susceptibility by obtaining steady-state solutions of the density matrix elements and averaging over the Maxwell-Boltzmann velocity distribution. For the σ^\pm components of the probe beam, the corresponding effective electric susceptibilities are given by

$$\chi_\pm = -N_{\text{Rb}} \frac{3\lambda^3}{4\pi^2} \cdot \frac{\Gamma}{\Omega_0} \cdot \frac{1}{\sqrt{\pi}u} \sum_{F_e=0}^2 \sum_{m=-F_g}^{F_g} \frac{C_{1,m}^{F_e, m\pm 1}}{a_\pm} \times \int_{-\infty}^{\infty} dv e^{-(v/u)^2} \langle F_e, m \pm 1 | \rho_{\text{pr}} | F_g, m \rangle, \quad (4)$$

where N_{Rb} is the atomic number density of rubidium in the cell, Γ is the decay rate of the excited state, $\Omega_0 = \mu_{\text{eg}} E_0 / \hbar$ is the Rabi frequency of the light beam (μ_{eg} : transition dipole matrix element), $u = \sqrt{2k_{\text{B}}T/M}$ is the most probable speed (k_{B} : Boltzmann constant, T : temperature of the cell, M : mass of an atom), ρ_{pr} is the density matrix elements related to interactions of the probe beam, and $C_{F_g, m_g}^{F_e, m_e}$ is the normalized transition strength between the states $|F_g, m_g\rangle$ and $|F_e, m_e\rangle$. The detailed derivation can be found in Section S1 in the Supporting Information. Thus, the atomic effective refractive index is

$$n_\pm = \sqrt{1 + \chi_\pm}. \quad (5)$$

Finally, combining the atomic response of the Rb vapor and optical response of the metasurface, we obtain the transmitted field of the hybrid cell:

$$\mathbf{E}_{\text{thru}} = \frac{E_0 t_x}{2} (a_- e^{in_- kl_c} - ia_+ e^{in_+ kl_c}) \hat{\mathbf{e}}_x + \frac{E_0 t_y}{2} (a_+ e^{in_+ kl_c} - ia_- e^{in_- kl_c}) \hat{\mathbf{e}}_y, \quad (6)$$

where t_x (t_y) are the complex transmission coefficients of TM (TE) polarized lights across the metasurface, and l_c is the length of the vapor cell. Using equations (1–6),

the atomic transmittance spectrum of the hybrid system can be obtained. In short, when the polarization of the incident light deviates from the eigenpolarizations of the metasurface (i.e., TM and TE polarizations), the reflected beam will be converted into elliptically polarized light. The following atomic transitions and populations will be simultaneously changed. Moreover, there are multiwaves mixing and Zeeman coherences in the multiphoton processes. As a result, the atomic polarization and optical coherence are highly dependent on the SOP of the incident light. Finally, the light passing through the atomic vapor will be endowed with these features, and the effective electric susceptibility of the vapor can be evaluated with equation (4).

D. Sub-Doppler atomic spectra

Figure 3c sketches the experimental setup to measure the transmittance and reflectance spectra of the hybrid device, where the vapor cell was heated to 60°C. In Fig. 3c, a tunable laser operating near 780 nm was used to sweep the wavelength of the incident light and linearly polarized by a polarizer. Then, a half-wave ($\lambda/2$) plate and a quarter-wave ($\lambda/4$) plate were used to vary the direction and ellipticity of light's polarization. Furthermore, a neutral density filter (NDF) was utilized to attenuate the laser beam power. With a focusing lens, the laser beams had circular profiles with diameters of approximately 0.3 mm when arriving at the metasurface, and the transmitted and reflected light beams were detected with photodiodes. It is important to note that weak focusing was employed to guarantee that the metasurface chip operates with zeroth-order reflection. Narrow the beam size to 0.3 mm to make sure that most of the field was reflected in the metasurface pattern. This adjustment can greatly minimize the side effects caused by metasurface pattern. Furthermore, we aimed to avoid having an excessively small beam size that would cause increased transit-time broadening.

First, we present the spectra of the linearly polarized light with varying polarization directions, which was accomplished by adjusting the optical axis angle ϑ of the $\lambda/2$ plate (without using the $\lambda/4$ plate). Figure 4a shows the measured transmission spectra for the transition of the Rb D2 line for the cases of 0° (TM), 90° (TE), and 45° linearly polarized incident beams with a power of 5 μ W (corresponding light intensity of 7 mW cm⁻¹). Due to the high polarization extinction ratio of the metasurface, the transmitted power increased when the incident beam changed from TM to TE polarization. Higher transmitted power leads to a better signal-to-noise ratio during the detection, which corresponds to a lower level of background noise in the measured spectra. The typical D2 line spectra of both ⁸⁷Rb and ⁸⁵Rb atoms can be observed in the main shapes of the Doppler broadening lineshape. Each line has a spectral width of approximately 570 MHz,

which includes a Doppler broadening width of 550 MHz, a natural linewidth of 6 MHz, and other broadening contributions such as a residual gas collision broadening and a limited interaction time between Rb atoms and the light beam. Specifically, the transmittance of the 45° linearly polarized light shows some differences compared with those of TM and TE polarized lights, where the spectra for the hyperfine transitions of ⁸⁷Rb $F_g = 1 \rightarrow F_e$ and ⁸⁵Rb $F_g = 2 \rightarrow F_e$ are clearly demonstrated. To further analyze these differences, we focused on observing the last hyperfine transition spectra (⁸⁷Rb $F_g = 1 \rightarrow F_e$) by adjusting the polarization direction of the incident light. Figure 4b shows the experimental results for different ϑ values of the $\lambda/2$ plate. Figure 4c displays the corresponding simulation results. There are obvious resemblances between simulated and measured transmittance spectra.

As shown in Fig. 4b, for both TM and TE polarized incident lights, the absorption spectra are similar to the spectrum of a single beam that passed through a vapor cell. Due to the weak intensity of the incident light, the VSOP effect is currently not functional in the present pump-probe configuration. However, in the case of non-eigenpolarization incidence, the optical coherence and interference between two circular components can be observed. Since the two eigenpolarization components have different complex reflection coefficients, the incident light is converted into elliptically polarized light when it is not pure TM or TE polarized. According to the characterization results of the metasurface, the magnitudes of r_x and r_y are 0.93 and 0.16, respectively, where there is a phase difference of 65°. In this pump-probe configuration, the left- and right-handed circular components will not be balanced in the pump beam. The corresponding σ^\pm transitions will also be affected. Specifically, via the transition of $F_g \rightarrow F_e \leq F_g$, the ground populations of Zeeman sublevels are tilted due to the unbalanced pumping of the reflected lights. The induced variations of the optical coherences can be explored by the probe beam. It is important to stress that the transmittance spectrum is not obtained by simply multiplying the atomic response with the incident light. Due to the linear dichroism of the metasurface, the TM/TE polarized components have very different transmission coefficients. The experimental results show that the magnitude of t_y is approximately 0.72, whereas that of t_x is less than 0.01. Consequently, the metasurface is almost transparent for the TE polarized light. Using equation (6), we observe that the overall transmittance is a result of the interference between left- and right-handed circular components, which incorporate the corresponding atomic responses (see Section S2, Supporting Information). Through these interactions, the sub-Doppler responses linked to the hyperfine structures can be resolved in our transmittance and reflectance spectra. The measured transmittance spectra in Fig. 4b show clear sub-Doppler absorption dips when ϑ is 5°, 10°, and 20°. The corresponding reflectance spectra are shown in Figure S4 in the Supporting Information, where the sub-Doppler features can also be observed. Hence, we have

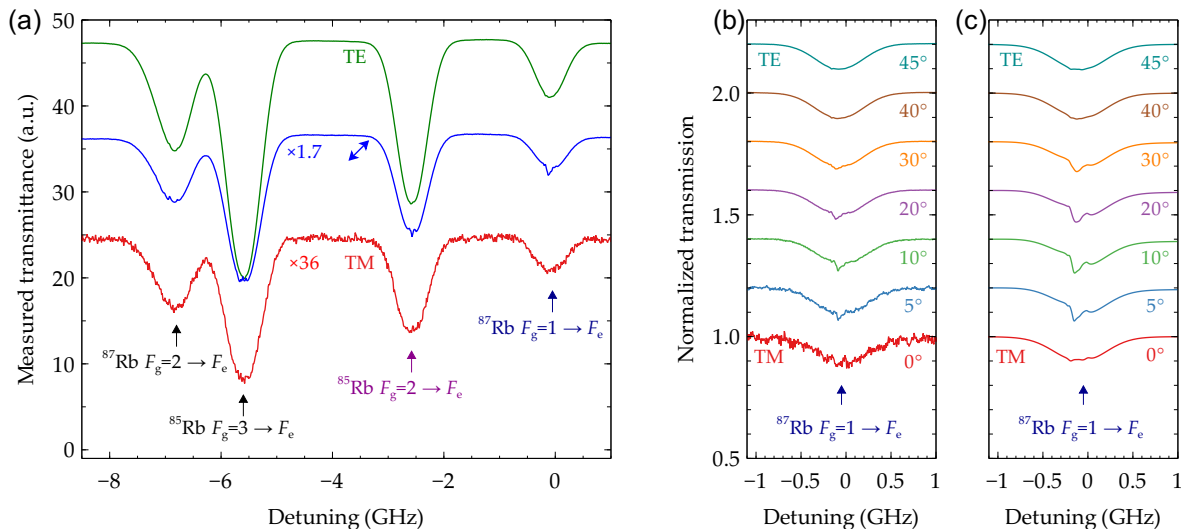


Figure 4. Transmittance spectra for linearly polarized incident lights. a) Experimental power transmissions for the D2 transition of Rb atoms at TM, TE, and 45° polarized incident beams. b) Measured and c) simulated results of normalized transmittance spectra for the transition of $^{87}\text{Rb } F_g = 1$ to $F_e = 0, 1, 2$ for different linearly polarized incident lights. The polarization direction of incident light is varied by changing the optical axis angle ϑ of the half-wave plate. $\vartheta = 0^\circ$ and 45° generate TM and TE polarized lights, respectively. In b) and c), spectrum curves for ϑ ranging from 0° to 45° are shown and shifted with a step of 0.2 in the y -axis to improve clarity.

shown that the polarization direction of linear polarized light can be utilized to tune the atomic spectra in our system.

E. Altering sub-Doppler lineshape

To further illustrate the impact of the SOP of the incident light beam, we adjusted the SOP of light by passing it through a cascade of a $\lambda/2$ plate and a $\lambda/4$ plate, as shown in Fig. 3c and Fig. 5a. Using this cascade setting, in principle, the SOP of light can be adjusted to any state by varying the optical axes of both plates. In our experiment, we set a fixed angle of 30° for the optical axis of the $\lambda/4$ plate. The optical axis angle ϑ of the $\lambda/2$ plate was varied to tune the SOP of incident light. These settings help the SOP evolve from linear polarization to circular polarization. Figure 5b shows the corresponding SOP trace with a blue dashed circle on the Poincaré sphere, where a cycle evolution can be achieved by a $\pi/2$ variation of ϑ . In the experiment, ϑ was varied from 0° to 90° ; Figure 5b also indicates the starting position of the SOP and the evolution direction. Figure 5c shows the measured results of the normalized transmittance spectra for the transitions of $^{87}\text{Rb } F_g = 1 \rightarrow F_e$. The sub-Doppler transparent peaks can be found at near circular polarizations of the incident light, as the curves of $\vartheta = 0^\circ$, 45° , and 90° in Fig. 5c show. In these cases, the incident light is nearly circularly polarized, whereas the reflected light is transferred to an elliptically polarized light. In other words, the probe light interacts with Rb atoms

solely through one of the σ^\pm transitions. In this pump-probe configuration, the transmittance spectrum exhibits its sub-Doppler feature in the transparent instead of the absorption. When the incident SOP is adjusted from the circular polarization to a linear polarization, the sub-Doppler transparent peaks will be converted to the sub-Doppler absorption dip ($\vartheta = 60^\circ$), where the maximum absorption is achieved (see Fig. 5c). This evolution of the sub-Doppler lineshape is analogous to the typical evolution for a two-path optical interference, where the dispersion is moderated by the incident SOP incorporated with the thermal atoms.

F. Power dependence and laser stabilization

To examine the effect of the beam intensity on the spectra, we performed experiments with different powers of the incident beam in the cases of circular polarization of the incident light. As shown in Fig. 6a, the transmission spectrum is changed by varying the power levels. The entire attenuation induced by the absorption of atoms decreased with the increase in power, which can be interpreted by the power dependence saturation mechanism of two-level systems. Meanwhile, the sub-Doppler lineshapes were altered due to the tuning of the incident light power level, since both effective probe and pump strength were changed. The sub-Doppler features for each hyperfine transition and VSOP spectroscopy are displayed at the higher incident power (see Figure S3, Supporting Information). However, there was a concurrent decrease in

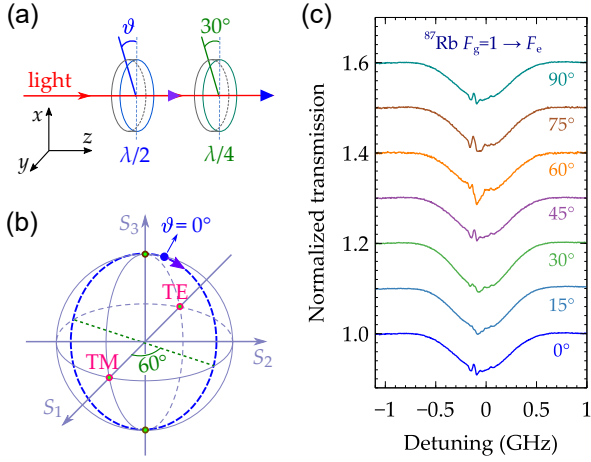


Figure 5. Experimental transmittance spectra for the incident lights with different SOPs. a) The SOP of the incident light was varied using a cascaded structure of a $\lambda/2$ plate and a $\lambda/4$ plate. In the experiment, the optical axis of the $\lambda/4$ plate was fixed with an angle of 30° , whereas the optical axis angle ϑ of the $\lambda/2$ plate was varied. b) The blue dashed circle on the Poincaré sphere is the corresponding trace of SOP with the operation in (a). A cycle trace will be formed for a $\pi/2$ variation of ϑ . For ϑ varying from 0° to 90° , the initial SOP location and evolution direction are marked on the circle. c) Normalized transmittance spectra for the transitions of $^{87}\text{Rb } F_g = 1 \rightarrow F_e$ for incident light with ϑ varying from 0° to 90° in a) and b). The spectrum curves are shifted with a step of 0.1 from $\vartheta = 0^\circ$ to 90° in the y -axis to improve clarity.

interference contrast. As the five curves in Fig. 6a show, the transparent peak has the best contrast at the power of $10 \mu\text{W}$. This sharp peak can be used to stabilize lasers. To demonstrate the stabilization performance of a laser, we performed the measurement with the experimental setup in Fig. 6b. The distributed feedback (DFB) laser was modulated by modulating the frequency of the injection current. The error signal was generated using the lock-in amplifier to demodulate the transmission signal of the hybrid vapor cell. Then, the error signal was added to adjust the injection current to stabilize the DFB laser. The wavelength of the DFB laser was recorded using a high-precision wavelength meter. Figure 6c shows the normalized Allan deviation of the measured laser wavelength. Compared with the free-running laser, the locked laser clearly shows better wavelength stabilization with the Allan deviation of 3×10^{-10} at 2 s, which may be limited by the resolution of the wavelength meter and the shifts in atomic energy levels as a background magnetic field.

III. DISCUSSION AND CONCLUSION

In this work, the sub-Doppler responses for atomic hyperfine transitions were observed using the metasurface-

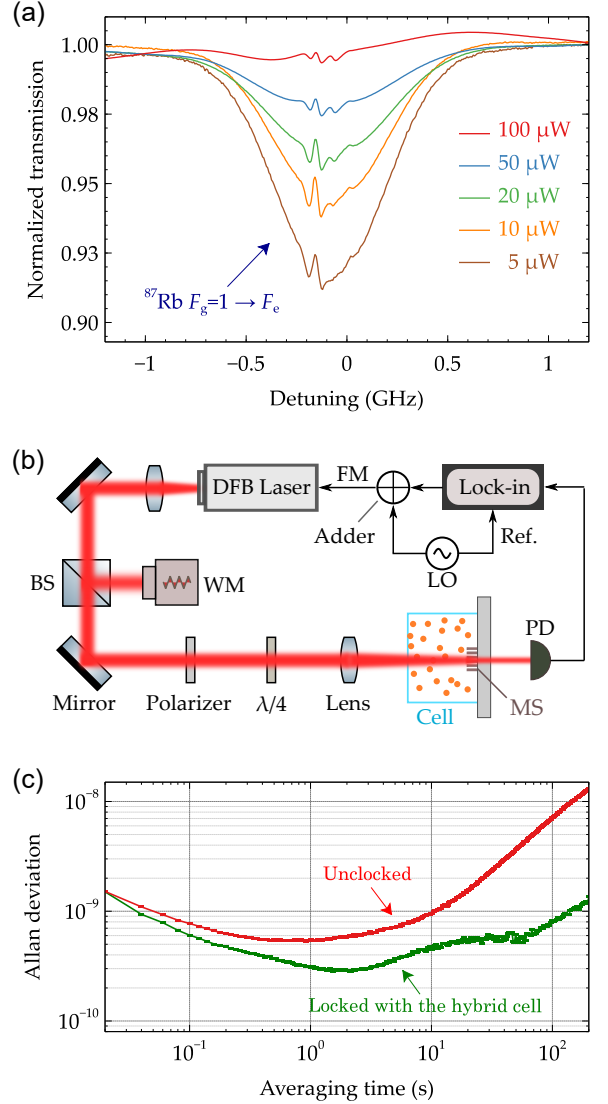


Figure 6. Power dependence of the transmittance spectra. a) Experimental normalized transmittance spectra for the transitions of $^{87}\text{Rb } F_g = 1 \rightarrow F_e$ at different powers of the incident beam. b) Measurement setup for the laser stabilization. The optical beams are shown in red wide lines. Electrical connections are shown in black arrows. DFB laser: distributed feedback laser; PA: piezoelectric actuator; WM: wavelength meter; FM: frequency modulation; LO: local oscillator. c) Allan deviations for the free-running DFB laser and stabilized DFB laser with the hybrid cell.

integrated hybrid cell in both transmissivity and reflectivity. These sub-Doppler spectra do not require high light intensity, which differs from the responses caused by the VSOP effect. In fact, the VSOP effect will appear in the sub-Doppler responses with the increase in incident power. Moreover, the sub-Doppler lineshape in our system can be altered by adjusting the SOP of the incident light. In the experiment, the transition from the sub-Doppler transparent peak-to-absorption dip was observed by changing the

circular polarization to a linear polarization of the incident light. These sub-Doppler spectra are the cooperation results of the atomic response of the thermal atoms and the optical response of the metasurface chip (see Section S2, Supporting Information).

To interpret the experimental spectra, we modeled this hybrid system, and the calculations are consistent with the measured results. However, some of the details of the sub-Doppler atomic spectra are not consistent, and there are several possible reasons. First, for the pump light, we did not consider the depletion of the probe light absorbed by the atoms, especially around the resonance. This depletion will affect the Rabi frequency of the pump beam, and the dispersion varies because the absorption depends on the frequency. Further improvements may be achieved by iterative calculations between optical fields and density matrix equations. Second, the transfer of ground populations from one hyperfine level to another is not considered. In our calculations, we assumed that the transitions between each ground hyperfine level to their excited states form a closed system, but this is not a true condition in Rb atoms. The transfer of ground populations of this type may be considered in future investigations. Third, the atom–surface interaction was not considered. In our hybrid cell, the metasurface structure can directly touch the atomic vapor. In this condition, the interaction between near-field photons and atoms can occur, which may cause further spectrum broadening due to the limited interaction time and frequency shifts of transitions induced by the Casimir–Polder interaction.[26, 40, 44, 45] In addition, the sub-Doppler lineshape is affected by the collisions between residual gas molecules and Rb atoms. The residual gas has buffering and quenching functions. Collisions with the residual gas can lead to a mixing of the Zeeman levels of the excited state, which change the populations of the Zeeman levels. The quenching process causes the atoms to return to their ground state without the emission of a resonance photon. By taking into account the impact of this population transfer between Zeeman levels and non-radiative transitions, more accurate calculations could be achieved. In our experiment, the vacuum level was not so good due to the limitation of the vacuum extractor. In fact, using our metasurface chip, the spectral linewidth of sub-Doppler responses can be reduced with a high vacuum vapor cell (see Figure S5, Supporting Information).

In summary, we engineered a nanograting metasurface with an operating wavelength that corresponded to the D2 line of Rb atoms. The fabricated metasurface chip was integrated with a miniature vapor cell. By utilizing the multifunction light control of the metasurface, we built a pump-probe configuration in the hybrid vapor cell and observed sub-Doppler spectra in our experiments. The lineshape of the sub-Doppler response can be tuned by changing the SOP of the incident light at low intensity. A spectrum transition from the absorption to the transparency was observed. Using one of the sub-Doppler transparent responses, the laser stabilization

with 3×10^{-10} instability at 2 s was achieved. Our study investigated the potential applications of optical metasurfaces in manipulating atomic spectra, which holds great promise for future advances in fundamental optics and innovative optical applications.

IV. EXPERIMENTAL SECTION

Device fabrication. First, the all-dielectric nanograting metasurface chip was fabricated. We used 1-mm-thickness borosilicate glass substrate, on which the silicon film with height of 290 nm was prepared by e-beam evaporation. Then the silicon nanogratings of 441 nm in pitch and 285 nm in width were patterned by e-beam lithography and dry etching. Second, a cubic quartz chamber with inter length of 10 mm was bonded to the prepared metasurface chip using low vapor pressure resin sealant. Then a rubidium (Rb) dispenser pill was inserted into the chamber, which was evacuated with vacuum degree less than 0.1 Pa and sealed successively. Finally, the Rb atoms were released by focusing a 915 nm semiconductor laser onto the pill for a time duration of 15 s at the power of 5 W. The hybrid metasurface-atomic-vapor cell was fabricated by using the above steps.

Measurement setup. The optical reflection of the metasurface structure was measured with illumination of a 780-nm tunable diode laser (Toptica DL pro) and detection of a photodiode (Thorlabs PDA36A2). The metasurface chip and the detector were mounted on two separated rotation stages to perform the measurements at different incident angles. The atomic reflectance and transmittance spectra of the hybrid cell were measured with the tunable laser and two photodiodes. In this optical setup, waveplates, variable aperture, lenses, neutral density filter, and beam splitters were used to adjust the polarizations, power, and profiles of the light beams. In the experiment of laser stabilization, a distributed feedback (DFB) laser (UniQuanta DFB801-780) was used for the stabilization demonstration. The frequency modulated DFB laser was controlled by adjusting the injection current with error signal, which was generated by the demodulation of the hybrid vapor cell transmission signal. A wavelength meter (HighFinesse WS-7) was used to measure the wavelength of the DFB laser.

Acknowledgements

This work is supported by the Fundamental Research Funds for the Central Universities under Grant KG21008401.

Conflict of Interest. The authors declare no conflict of interest.

Data Availability Statement. The data that support the findings of this study are available from the corresponding author upon reasonable request.

Supporting Information. Supporting Information is available from the Wiley Online Library or from the author.

- [1] Ludlow, A. D., Boyd, M. M., Ye, J., Peik, E. & Schmidt, P. Optical atomic clocks. *Rev. Mod. Phys.* **87**, 637–701 (2015).
- [2] Camparo, J. The rubidium atomic clock and basic research. *Phys. Today* **60**, 33–39 (2007).
- [3] Diddams, S. A., Bergquist, J. C., Jefferts, S. R. & Oates, C. W. Standards of time and frequency at the outset of the 21st century. *Science* **306**, 1318–1324 (2004).
- [4] Kitching, J., Knappe, S. & Donley, E. A. Atomic sensors – A review. *IEEE Sens. J.* **11**, 1749–1758 (2011).
- [5] Fang, J. & Qin, J. Advances in atomic gyroscopes: A view from inertial navigation applications. *Sensors* **12**, 6331–6346 (2012).
- [6] Kominis, I. K., Kornack, T. W., Allred, J. C. & Romalis, M. V. A subfemtotesla multichannel atomic magnetometer. *Nature* **422**, 596–599 (2003).
- [7] Budker, D. & Romalis, M. Optical magnetometry. *Nat. Phys.* **3**, 227–234 (2007).
- [8] Bize, S. *et al.* Cold atom clocks and applications. *J. Phys. B: At. Mol. Opt. Phys.* **38**, S449–S468 (2005).
- [9] Hong, F.-L. Optical frequency standards for time and length applications. *Meas. Sci. Technol.* **28**, 012002 (2016).
- [10] Pearman, C. P. *et al.* Polarization spectroscopy of a closed atomic transition: Applications to laser frequency locking. *J. Phys. B: At. Mol. Opt. Phys.* **35**, 5141–5151 (2002).
- [11] Boto, E. *et al.* Moving magnetoencephalography towards real-world applications with a wearable system. *Nature* **555**, 657–661 (2018).
- [12] Maguire, L. P., van Bijnen, R. M. W., Mese, E. & Scholten, R. E. Theoretical calculation of saturated absorption spectra for multi-level atoms. *J. Phys. B: At. Mol. Opt. Phys.* **39**, 2709–2720 (2006).
- [13] Moon, G. & Noh, H.-R. Analytic calculation of linear susceptibility in velocity-dependent pump-probe spectroscopy. *Phys. Rev. A* **78**, 032506 (2008).
- [14] Zigdon, T., Wilson-Gordon, A. D. & Friedmann, H. Absorption spectra for strong pump and probe in atomic beam of cesium atoms. *Phys. Rev. A* **80**, 033825 (2009).
- [15] Harris, M. L. *et al.* Polarization spectroscopy in rubidium and cesium. *Phys. Rev. A* **73**, 062509 (2006).
- [16] Brazhnikov, D. V., Taichenachev, A. V. & Yudin, V. I. Polarization method for controlling a sign of electromagnetically-induced transparency/absorption resonances. *Eur. Phys. J. D* **63**, 315–325 (2011).
- [17] Brazhnikov, D. V. *et al.* High-quality electromagnetically-induced absorption resonances in a buffer-gas-filled vapour cell. *Laser Phys. Lett.* **15**, 025701 (2018).
- [18] Rehman, H.-u., Adnan, M., Noh, H.-R. & Kim, J.-T. Spectral features of electromagnetically induced absorption in ^{85}Rb atoms. *J. Phys. B: At. Mol. Opt. Phys.* **48**, 115502 (2015).
- [19] Krasteva, A. *et al.* Observation and theoretical simulation of electromagnetically induced transparency and enhanced velocity selective optical pumping in cesium vapour in a micrometric thickness optical cell. *J. Phys. B: At. Mol. Opt. Phys.* **47**, 175004 (2014).
- [20] Rehman, H. U., Mohsin, M. Q., Noh, H.-R. & Kim, J.-T. Electromagnetically induced absorption due to transfer of coherence and coherence population oscillation for the $F_g=3 \rightarrow F_e=4$ transition in ^{85}Rb atoms. *Opt. Commun.* **381**, 127–134 (2016).
- [21] Budker, D. *et al.* Resonant nonlinear magneto-optical effects in atoms. *Rev. Mod. Phys.* **74**, 1153–1201 (2002).
- [22] Overvig, A. C. *et al.* Dielectric metasurfaces for complete and independent control of the optical amplitude and phase. *Light Sci. Appl.* **8**, 92 (2019).
- [23] Kamali, S. M., Arbabi, E., Arbabi, A. & Faraon, A. A review of dielectric optical metasurfaces for wavefront control. *Nanophotonics* **7**, 1041–1068. (2018).
- [24] Yu, N. *et al.* Light propagation with phase discontinuities: Generalized laws of reflection and refraction. *Science* **334**, 333–337 (2011).
- [25] Rubin, N. A., Shi, Z. & Capasso, F. Polarization in diffractive optics and metasurfaces. *Adv. Opt. Photon.* **13**, 836 (2021).
- [26] Achouri, K. & Caloz, C. Design, concepts, and applications of electromagnetic metasurfaces. *Nanophotonics* **7**, 1095–1116 (2018).
- [27] Chen, Z. & Segev, M. Highlighting photonics: looking into the next decade. *eLight* **1**, 2 (2021).
- [28] Bao, Y., Ni, J. & Qiu, C.-W. A minimalist single-layer metasurface for arbitrary and full control of vector vortex beams. *Adv. Mater.* **32**, 1905659 (2019).
- [29] Overvig, A. C., Malek, S. C. & Yu, N. Multifunctional Nonlocal Metasurfaces. *Phys. Rev. Lett.* **125**, 017402 (2020).
- [30] Feng, Z. *et al.* Dual-band polarized upconversion photoluminescence enhanced by resonant dielectric metasurfaces. *eLight* **3**, 21 (2023).
- [31] Wang, S., Wen, S., Deng, Z.-L., Li, X. & Yang, Y. Metasurface-based solid Poincaré sphere polarizer. *Phys. Rev. Lett.* **130**, 123801 (2023).
- [32] Bar-David, J., Stern, L. & Levy, U. Dynamic Control over the Optical Transmission of Nanoscale Dielectric Metasurface by Alkali Vapors. *Nano Lett.* **17**, 1127–1131 (2017).
- [33] Sebbag, Y., Talker, E., Naiman, A., Barash, Y. & Levy, U. Demonstration of an integrated nanophotonic chip-scale alkali vapor magnetometer using inverse design. *Light Sci. Appl.* **10**, 54 (2021).
- [34] Yang, X., Benelajla, M., Carpenter, S. & Choy, J. T. Analysis of atomic magnetometry using metasurface optics for balanced polarimetry. *Opt. Express* **31**, 13436–13446 (2023).
- [35] Xu, Y. *et al.* Atomic spin detection method based on spin-selective beam-splitting metasurface. *Adv. Optical Mater.* 2301353 (2023).
- [36] Hummon, M. T. *et al.* Photonic chip for laser stabilization to an atomic vapor with 10^{-11} instability. *Optica* **5**, 443 (2018).
- [37] Zhu, L. *et al.* A dielectric metasurface optical chip for the generation of cold atoms. *Sci. Adv.* **6**, eabb6667 (2020).
- [38] Ropp, C. *et al.* Integrating planar photonics for multi-beam generation and atomic clock packaging on chip. *Light Sci. Appl.* **12**, 83 (2023).
- [39] Aljunid, S. A. *et al.* Atomic response in the near-field of nanostructured plasmonic metamaterial. *Nano Lett.* **16**, 3137–3141 (2016).
- [40] Chan, E. A. *et al.* Tailoring optical metamaterials to tune the atom-surface casimir-polder interaction. *Sci. Adv.* **4**, eaao4223 (2018).

- [41] Karagodsky, V., Sedgwick, F. G. & Chang-Hasnain, C. J. Theoretical analysis of subwavelength high contrast grating reflectors. *Opt. Express* **18**, 16973 (2010).
- [42] Chang-Hasnain, C. J. & Yang, W. High-contrast gratings for integrated optoelectronics. *Adv. Opt. Photon.* **4**, 379 (2012).
- [43] Qiao, P., Yang, W. & Chang-Hasnain, C. J. Recent advances in high-contrast metastructures, metasurfaces, and photonic crystals. *Adv. Opt. Photon.* **10**, 180–245 (2018).
- [44] Stern, L., Desiatov, B., Goykhman, I. & Levy, U. Nanoscale light–matter interactions in atomic cladding waveguides. *Nat. Commun.* **4**, 1548 (2013).
- [45] Ritter, R. *et al.* Coupling Thermal Atomic Vapor to Slot Waveguides. *Phys. Rev. X* **8**, 021032 (2018).